Supporting information

S1. Model verification

The BioRT-Flux-PIHM 1.0 was verified against the benchmark CrunchTope, which is a widely used subsurface reactive transport model (Steefel and Lasaga, 1994;Steefel et al., 2015). Due to the limitation of CrunchTope in representing complex terrain and land-surface process, verification is performed under simplified hydrological conditions with 1-D column and constant flow rates such that it focuses on biogeochemical reactive transport processes such as advection, diffusion, dispersion, and biogeochemical reactions. Specifically, three cases of soil phosphorus, carbon, and nitrogen were verified for temporal evolution and spatial pattern of relevant solute concentrations (Figure S1 – S7). The soil phosphorus case, which involves geochemically kinetic and thermodynamic processes (i.e., apatite dissolution and phosphorous speciation), was first tested for the solution accuracy of the bulk code that was inherited from the original RT-Flux-PIHM. Soil carbon and nitrogen cases that involve microbially driven processes, such as soil carbon decomposition and mineralization, nitrification and denitrification, were further verified for the solution accuracy of the augmented BioRT module.

For the physical context, two transport scenarios were set up in the 1D column (i.e., 100 grids × 0.1 m) with a constant flow rate of 2 m/d, i.e., advection-only case and advection + diffusion + dispersion case (Table S1).

Table S1. Flow and transport setup in the verification

# of grid	Grid size (m)	Flow rate (m/d)	Advection-only case		Advection + diffusion + dispersion	
			Diffusion coefficient (cm^2/s)	Dispersivity (m)	Diffusion coefficient (cm^2/s)	Dispersivity (m)
100	0.1	2	1.0×10^{-20}	1.0×10^{-20}	1.0×10^{-5}	0.1

S1.1. Soil phosphorus processes

Reaction network includes one kinetically controlled P-containing mineral dissolution (i.e., apatite) and three thermodynamically controlled phosphorus speciation reactions (Figure S1). The conservative tracer Cl is additionally included in the simulation for testing non-reactive transport processes.
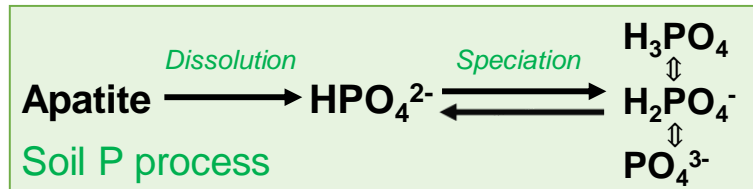
Figure S1. Soil phosphorus processes in the CrunchTope verification.

In the advection-only case where diffusion coefficient (1.0×10^{-20} cm^2/s) and dispersivity (1.0×10^{-20} m) are set to be negligible, we test the code's ability to capture the sharp concentration front of phosphorus species. In the other case, diffusion and dispersion processes are included with diffusion coefficient (1.0×10^{-5} cm^2/s) and dispersivity (0.1 m) while maintaining all other flow and geochemical conditions the same as the advection-only case (Table S1). That is, in both cases, the columns are initially set up at conditions of pH = 6.0, Cl$^-$ = 1.0×10^{-4} (mol/L), HPO$_4^{2-}$ = 1.0×10^{-7} (mol/L), Ca^{2+} = 1.0×10^{-7} (mol/L), apatite = 1% (volume fraction), porosity = 0.4. The injection condition is set up as pH = 4.0, Cl = 1.0×10^{-3} (mol/L), HPO$_4^{2-}$ = 1.0×10^{-5} (mol/L), Ca^{2+} = 1.0×10^{-5} (mol/L). The phosphorous reaction network with kinetic and thermodynamic parameters are summarized in Table S2.

Table S2. Soil phosphorous reaction in the CrunchTope verification

Phosphorous reaction	Equation	Log$_{10}$k (mol/m^2/s)	Log$_{10}$K$_{eq}$
Apatite dissolution	$Ca_5(PO_4)_3(OH) + 4H^+$ $\rightleftharpoons 5Ca^{2+} + 3HPO_4^{2-} + H_2O$	-11.0	-3.07
Phosphorous speciation	$H_3PO_4 \rightleftharpoons H^+ + H_2PO_4^-$		-2.17
	$H_2PO_4^- \rightleftharpoons H^+ + HPO_4^{2-}$		-7.21
	$HPO_4^{2-} \rightleftharpoons H^+ + PO_4^{3-}$		-12.1

44   Modeling results show that the code BioRT-Flux-PIHM was able to reproduce
45   CrunchTope results under different flow conditions (Figure S2). That is, BioRT-Flux-PIHM
46   captured both the sharp concentration front in the advection-only case (Figure S2a, c)
47   and the smooth concentration front in the advection + diffusion + dispersion case (Figure
48   S2b, d). The close match of non-reactive Cl^- in the temporal and spatial trend indicates a
49   robust accuracy of transport code under varying flow conditions. Result consistencies in
50   the temporal evolution and spatial pattern of H^+ and total dissolved phosphorus (TP)
51   concentration suggest a valid implementation of kinetic reaction (i.e., apatite dissolution)
52   in the reaction code.
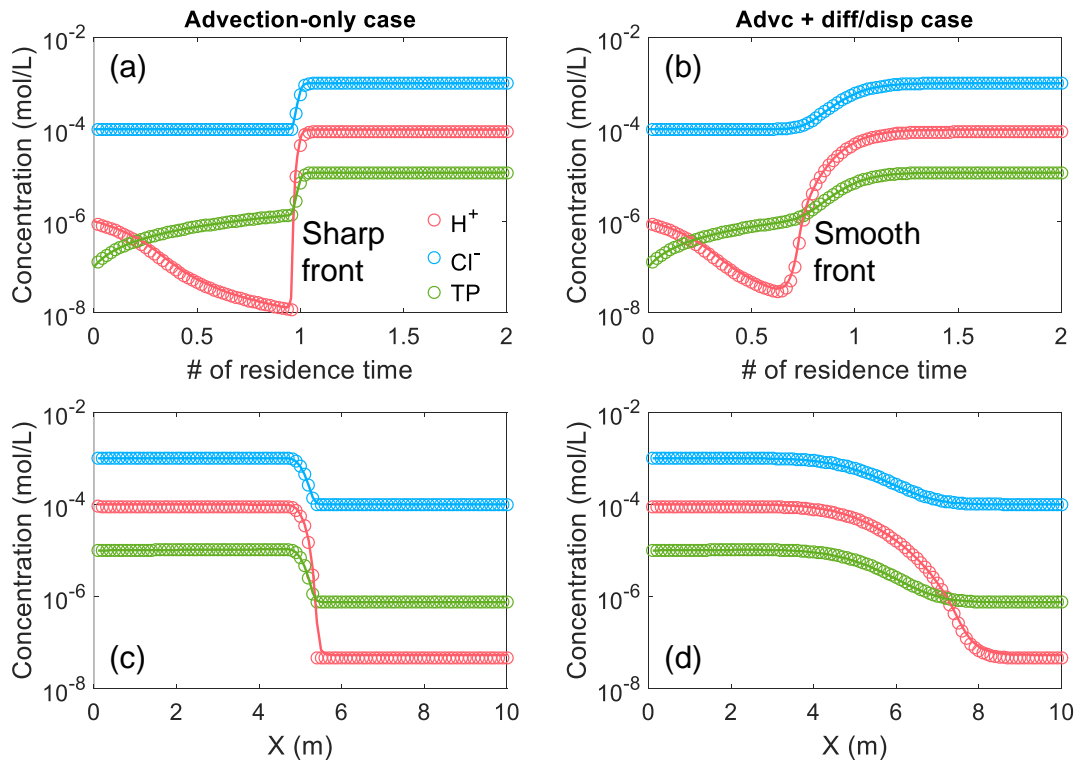
53
54   **Figure S2.** Soil phosphorus verification under advection case (left column) and advection +
55   diffusion + dispersion case (right column). Temporal evolution of solutes plotted at the column
56   outlet (a, b) and spatial pattern plotted at one residence time (c, d). Circle markers are BioRT-
57   Flux-PIHM results, while solid lines are CrunchTope results. The close match of BioRT-Flux-PIHM
58   and CrunchTope results indicates a robust accuracy.

59
60   Phosphate reaction was also validated against CrunchTope under two transport
61   cases (Figure S3). Phosphate speciation (i.e., fractions of H_3PO_4, $H_2PO_4^-$, HPO_4^{2-}, PO_4^{3-}

62 to TP) is a function of solution pH. The consistency of phosphate partitioning results

63 suggests that the implementation of aqueous speciation code in the reaction module is

64 robust under different pH conditions. In summary, the soil phosphorus case demonstrates

65 that the BioRT-Flux-PIHM maintains a robust accuracy in simulating both geochemical

66 kinetic and thermodynamic reactions under varying transport conditions.
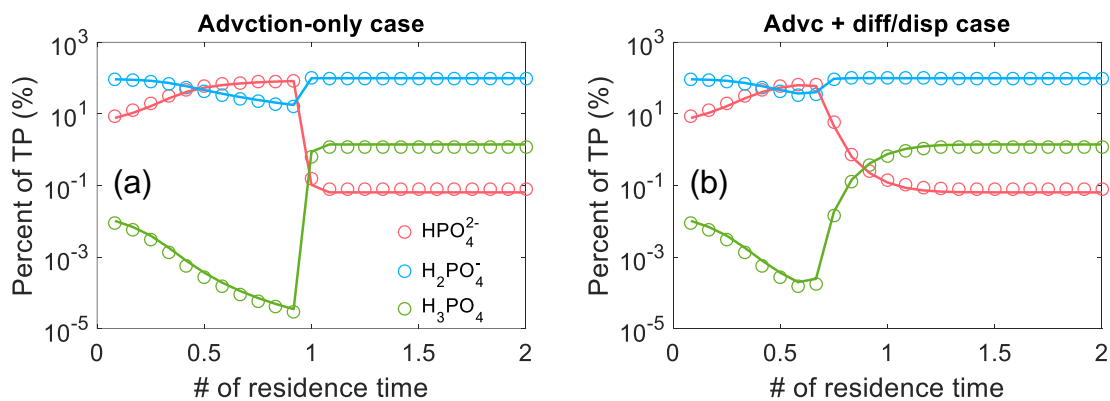
67

68 **Figure S3.** Phosphate chemistry verification under advection case (a) and advection + diffusion

69 + dispersion case (b). Orthophosphate (i.e., PO_4^{3-}) is ignored in the plot due to its extreme low

70 concentration. Circles are BioRT-Flux-PIHM results, while solid lines are CrunchTope results. The

71 close match of BioRT-Flux-PIHM and CrunchTope results indicates a robust accuracy.

72

73 **S1.2. Soil carbon processes**

74 Simulated carbon processes include soil organic carbon (SOC) decomposition and

75 dissolved organic carbon (DOC) mineralization (Figure S4). Both these soil carbon

76 processes are microbially-mediated reactions following the Monod rate law (Eq. (15)).

77 Soil temperature is set at 20 °C. A variety of different electron acceptors (i.e., O_2, NO_3^-,

78 SO_4^{2-}) are tested in the mineralization process to verify the code's implementation of

79 parallel reaction pathways. BioRT-Flux-PIHM is designed to model multiple microbially-

80 mediated reactions and their interactions under dynamic redox conditions; thus, it is

81 critical to reproducing redox ladder geochemistry (Figure S5a).
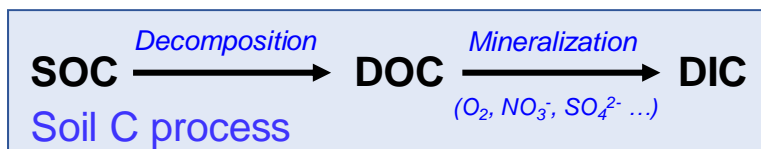
82

83 **Figure S4.** Soil carbon processes in the CrunchTope verification.

84

85   Detailed reaction network and reaction rate expressions of soil carbon processes

86 are summarized in the following Table S3. For simplification, half-saturation constants K

87 of different electron donors or electron acceptors are kept the same as 1.5×10^{-5} (mol/L).

88 The inhibition constant of $I_{O_2(aq)}$ and $I_{NO_3^-}$ are set as 1.5×10^{-5} (mol/L) and 1.5×10^{-6}

89 (mol/L), respectively. The chemical setup of the initial and injection conditions is listed in

90 the following Table S4.

91   **Table S3.** Simulated soil carbon reactions in the verification case

Reaction	Equation	Reaction rate expression	Rate const (log$_{10}$)
SOC decomposition	$CH_2O(s) \rightarrow CH_2O(aq)$	$k_{CH_2O(s)} A_{CH_2O(s)} X_{mio}$ $\dfrac{C_{CH_2O(s)}}{C_{CH_2O(s)} + K_{CH_2O(s)}}$	-11.0
Mineralization	$CH_2O(aq) + O_2(aq)$ $\rightarrow HCO_3^- + H^+$	$\kappa_{max,O_2(aq)} X_{mio} \dfrac{C_{CH_2O(aq)}}{C_{CH_2O(aq)} + K_{CH_2O(aq)}}$ $\dfrac{C_{O_2(aq)}}{C_{O_2(aq)} + K_{O_2(aq)}}$	-10.0
	$CH_2O(aq) + 0.8NO_3^-$ $\rightarrow HCO_3^- + 0.4N_2(aq)$ $+0.2H^+ + 0.4H_2O$	$\kappa_{max,NO_3^-} X_{mio} \dfrac{C_{CH_2O(aq)}}{C_{CH_2O(aq)} + K_{CH_2O(aq)}}$ $\dfrac{C_{NO_3^-}}{C_{NO_3^-} + K_{NO_3^-}} \dfrac{I_{O_2(aq)}}{I_{O_2(aq)} + C_{O_2(aq)}}$	-10.3
	$CH_2O(aq) + 0.5SO_4^{2-}$ $\rightarrow HCO_3^- + 0.5H_2S(aq)$	$\kappa_{max,SO_4^{2-}} X_{mio} \dfrac{C_{CH_2O(s)}}{C_{CH_2O(s)} + K_{CH_2O(s)}}$ $\dfrac{C_{SO_4^{2-}}}{C_{SO_4^{2-}} + K_{SO_4^{2-}}} \dfrac{I_{O_2(aq)}}{I_{O_2(aq)} + C_{O_2(aq)}}$ $\dfrac{I_{NO_3^-}}{I_{NO_3^-} + C_{NO_3^-}}$	-11.0

92

93

94

95

        Table S4. Initial and injection conditions in the soil carbon verification case

Species	Initial (mol/L)	Injection (mol/L)	Species (continued)	Initial (mol/L)	Injection (mol/L)
pH	6.0	4.0	SO_4^{2-}	3.0×10^{-5}	3.0×10^{-8}
$CH_2O(aq)$	1.0×10^{-8}	1.0×10^{-8}	HCO_3^-	1.0×10^{-8}	1.0×10^{-8}
$O_2(aq)$	3.0×10^{-5}	3.0×10^{-8}	$N_2(aq)$	1.0×10^{-8}	1.0×10^{-8}
NO_3^-	3.0×10^{-5}	3.0×10^{-8}	$H_2S(aq)$	1.0×10^{-8}	1.0×10^{-8}

Model results show that BioRT-Flux-PIHM closely matched CrunchTope results in both temporal evolution and spatial pattern of a variety of chemical species (Figure S5). The concentration profile of HCO_3^- (yellow), which is the sum of three DOC mineralization reactions, demonstrates that BioRT-Flux-PIHM is capable of solving parallel microbially-mediated redox reactions. It is worth mentioning that O_2 (red) was consumed first and fast among all three electron acceptors (i.e., O_2, NO_3^-, SO_4^{2-}). Following O_2 dynamic, the NO_3^- (green) was consumed slowly at the beginning when O_2 was still present, but the NO_3^- consumption became much faster once the O_2 was depleted and its inhibitory effect on NO_3^- disappears. The same consumption pattern also applies for the SO_4^{2-} (blue), which was consumed very slowly at the beginning when both O_2 and NO_3^- inhibited the SO_4^{2-} reaction. However, SO_4^{2-} was consumed much faster when O_2 and NO_3^- disappeared along with their inhibitory efforts. Such reaction sequence from model results essentially reproduced redox ladder biogeochemistry (inserted figure in Figure S6a), where top ladder reactions occur preferentially due to their higher redox potentials. In other words, soil microbes preferentially choose a redox reaction of DOC that most energy can be harvested. The spatial pattern of carbon solutes and other electron acceptors (Figure S5b) also show consistent results with CrunchTope. In short, both temporal and spatial patterns show consistent results with the benchmark CrunchTope regarding soil carbon decomposition and mineralization processes, suggesting the Monod rate law (e.g., substrate and inhibition terms) and environmental dependency (e.g., soil temperature) was correctly implemented.
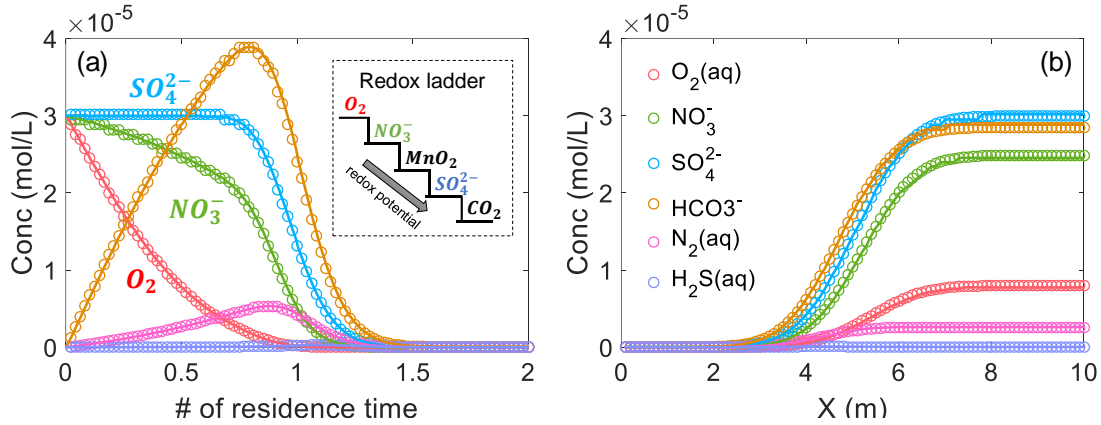
119

120 **Figure S5.** Soil carbon process verification at the column outlet (a) and at one residence time (b).

121 The embedded plot of the redox ladder is to demonstrate the code's ability to handle multiple

122 microbially-mediated reaction pathways under complex redox conditions. Circle markers are

123 BioRT-Flux-PIHM results while solid lines are CrunchTope results.

124

S1.3. Soil nitrogen processes

126   Simulated N processes include mineralization of dissolved organic nitrogen (DON)

127 to ammonium (NH_4^+), subsequent nitrification converting NH_4^+ to nitrate (NO_3^-), and

128 followed by denitrification reducing NO_3^- to N_2 (Figure S7). Similar to soil carbon, all these

129 sequential nitrogen transformations are microbial processes and follow the Monod rate

130 law (Eq. (15)). Soil temperature is set at 20 °C and soil nitrogen verification was performed

131 under the full transport condition of advection + diffusion + dispersion.
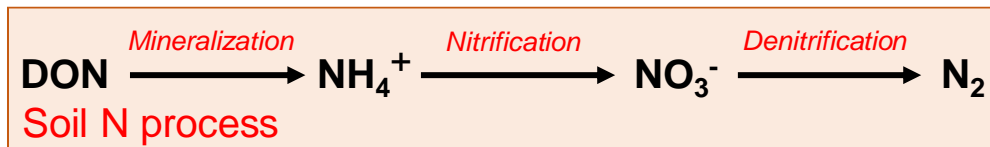
132

133   **Figure S6.** Soil nitrogen processes in the CrunchTope verification.

134

135   Detailed reaction network and reaction rate expressions of soil nitrogen processes

136 are summarized in Table S5. Half-saturation constants are as follows: K_{RNH_2} = 1.5 × 10^{-5}

137 (mol/L), $K_{O_2(aq)}$ = 1.5 × 10^{-5} (mol/L), $K_{NH_4^+}$ = 3.0 × 10^{-5} (mol/L), $K_{O_2(aq)}$ = 4.5 × 10^{-5} (mol/L).

138 The inhibition constant $I_{O_2(aq)}$ is set as 3.0 × 10^{-5} (mol/L). The chemical setup of the initial

139 and injection condition is listed in Table S6.

Table S5. Simulated soil nitrogen reactions in the verification case

Reaction	Equation	Reaction rate terms	Rate constant (log$_{10}$)
Mineralization	$RNH_2 + O_2(aq) + H_2O$ $\rightarrow NH_4^+ + ROH + OH^-$	$\kappa_{max,RNH_2} X_{mio} \dfrac{C_{RNH_2}}{C_{RNH_2} + K_{RNH_2}}$ $\dfrac{C_{O_2(aq)}}{C_{O_2(aq)} + K_{O_2(aq)}}$	-10.0
Nitrification	$NH_4^+ + 2O_2(aq) \rightarrow$ $NO_3^- + 2H^+ + 2H_2O$	$\kappa_{max,NH_4^+} X_{mio} \dfrac{C_{NH_4^+}}{C_{NH_4^+} + K_{NH_4^+}}$ $\dfrac{C_{O_2(aq)}}{C_{O_2(aq)} + K_{O_2(aq)}}$	-10.0
Denitrification	$CH_2O + 0.8NO_3^- \rightarrow$ $HCO_3^- + 0.4N_2(aq)$ $+ 0.2H^+ + 0.4H_2O$	$\kappa_{max,NO_3^-} X_{mio} \dfrac{C_{CH_2O}}{C_{CH_2O} + K_{CH_2O}}$ $\dfrac{C_{NO_3^-}}{C_{NO_3^-} + K_{NO_3^-}} \dfrac{I_{O_2(aq)}}{I_{O_2(aq)} + C_{O_2(aq)}}$	-11.0

Table S6. Initial and injection conditions in the soil nitrogen verification case

Species	Initial (mol/L)	Injection (mol/L)	Species (continued)	Initial (mol/L)	Injection (mol/L)
pH	6.0	4.0	NO$_3^-$	3.0 × 10^{-5}	3.0 × 10^{-8}
O$_2$(aq)	3.0 × 10^{-5}	3.0 × 10^{-8}	HCO$_3^-$	1.0 × 10^{-5}	1.0 × 10^{-5}
NH$_4^+$	1.0 × 10^{-8}	1.0 × 10^{-8}	N$_2$(aq)	1.0 × 10^{-8}	1.0 × 10^{-8}

 Model results show that BioRT-Flux-PIHM closely matched CrunchTope results in
 both temporal evolution and spatial pattern of a variety of nitrogen species (Figure S7).
 Products of NH$_4^+$, NO$_3^-$, and N$_2$(aq), which mainly originates from soil organic nitrogen in
 a forest-type land (no fertilizer), are sensitive to redox conditions as nitrification is an
 aerobic process while denitrification occurs largely under anoxic conditions. The O$_2$(aq)
 (red) was consumed (decreasing) both by the mineralization for production of NH$_4^+$
 (green) and by the nitrification for production of NO$_3^-$ (blue). The depletion of O$_2$(aq)
 decreased the production of NH$_4^+$ and NO$_3^-$; however, it facilitated the generation of

152 $N_2(aq)$ (purple) via the denitrification process. The spatial patterns of nitrogen species

153 (Figure S7b) also show the same results as the CrunchTope. The nitrogen case

154 demonstrates the code capability to model sequential microbial processes under dynamic

155 redox conditions.
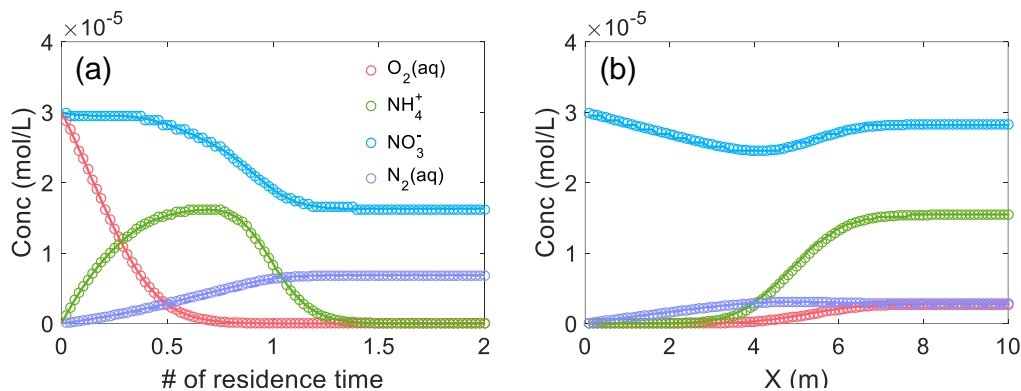
156

157 **Figure S7.** Soil nitrogen process verification at the column outlet (a) and at one residence time

158 (b). Circles are BioRT-Flux-PIHM results, while solid lines are CrunchTope results.

159

160 **S2. Rooting density function**

161 A rooting density function (Eq. (26)) was exponentially fitted based on field

162 measurement of root density distribution over depth at the Shale Hills watershed

163 (Hasenmueller et al., 2017).

164
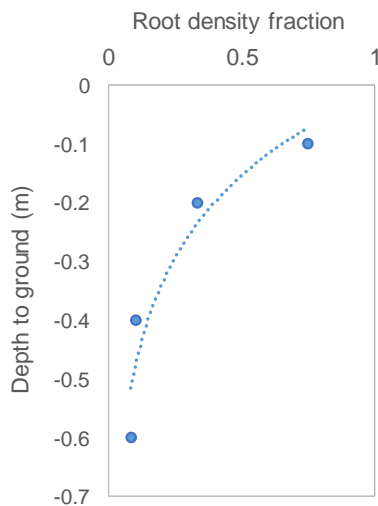
 Figure S8. Rooting density fraction as a function of soil depth based on Shale Hills measurement
166 (Hasenmueller et al., 2017). Dots are normalized data of root intersection density (count/m^2) while
167 the dashed line is the fitted function (Eq. (26), $R^2 = 0.90$).

168

169 **S3. Key parameters for hydrology and stream nitrate calibration at Shale Hills**

170   The model assumed a uniform soil type of the Weikert soil due to its dominance at
171 Shale Hills (Shi et al., 2013). For the deep zone, hydraulic properties were also assumed
172 to be uniform in the watershed. The deep zone porosity was set to 1/10 of the Weikert
173 soil porosity (Brantley et al., 2018;Kuntz et al., 2011). Hydrology was calibrated to
174 reproduce stream discharge and evapotranspiration (ET) (Figure S9). Deep groundwater
175 (Q_G) from the deep zone was constrained by the previous work (Li et al., 2017) and the
176 concentration-discharge (C-Q) dynamics of nitrate in this work. Important land surface
177 and hydrological parameters of shallow and deep zones are summarized in the following
178 Table S7.

179   **Table S7.** Key parameters for hydrology calibration at Shale Hills

Parameters	Symbols	Value	Note
Land surface	C_{zil}	0.19	Zilitinkevich coefficient
	HS	59	Water vapor exchange coefficient
	RS	177	Minimum stomatal resistance (s/m)
	$WLTSMC$	0.062	Wilting point
Shallow zone properties	$K_{satH}^{shallow}$	6.86	Horizontal saturated hydraulic conductivity (m/d)
	$K_{satV}^{shallow}$	1.21	Vertical saturated hydraulic conductivity (m/d)
	$K_{macH}^{shallow}$	4,805	Macropore horizontal hydraulic conductivity (m/d)
	$K_{macV}^{shallow}$	149	Macropore vertical hydraulic conductivity (m/d)
	D_{mac}	1.6	Macropore depth (m)

	$\theta_s^{shallow}$	0.12	Shallow zone porosity (m³/m³)
	α	8.45	Shallow zone van Genuchten alpha, inversely proportional to pore diameter (m⁻¹)
	n	1.19	Shallow zone van Genuchten n, inversely proportional to water retention
	$D_{shallow}$	1.96	Shallow zone thickness (m)
Deep zone properties	K_{satH}^{deep}	0.48	Deep horizontal saturated hydraulic conductivity (m/d)
	K_{satV}^{deep}	0.078	Deep vertical saturated hydraulic conductivity (m/d)
	θ_s^{deep}	0.012	Deep zone porosity (m³/m³)
	α	1.22	Deep zone van Genuchten n, inversely proportional to water retention (m⁻¹)
	n	1.92	Deep zone van Genuchten n, inversely proportional to water retention
	D_{deep}	10	Deep zone thickness (m)

180

For microbial soil N leaching and denitrification, reaction rate constant k was specified (Regnier and Steefel, 1999) and the lumped surface area A (m², = specific surface area m²/g $\times$ g of mass) was turned to reproduce stream nitrate dynamics and its C-Q pattern (Table S8). The calibrated effective specific surface area (SSA) were orders of magnitude lower than the lab measured SSA of natural materials (e.g., SOM, 0.6 ~ 2 m²/g (Rutherford et al., 1992;Chiou et al., 1990)). Such discrepancies between calibrated effective reactive surface area (i.e., solid-water contact area) and lab measured absolute surface area is consistent with other observations (Li et al., 2014;Heidari et al., 2017). The nitrate uptake rate constant k_{uptake} was calibrated to constrain the partitioning of N transformation flux between denitrification and plant uptake by the ratio of 1:5, a value estimated from field measurements of gaseous N outputs (3.53 kg-N/ha/yr) and plant N uptake (18.3 kg-N/ha/yr) (Weitzman and Kaye, 2018). We assumed the nitrate uptake

193 rate k_{uptake} of the deep zone (> 2 m in depth) was 1/1000 of that in the shallow zone,
194 based on the observations that the rooting density exponentially decrease with depth
195 (Weitzman and Kaye, 2018;Hasenmueller et al., 2017). Groundwater nitrate was
196 initialized as 0.43 mg/L, the average of measured groundwater concentration during
197 2009-2010.

198 **Table S8.** Key parameters for nitrate calibration at Shale Hills watershed

Reaction	Log rate constant	Specific surface area (m^2/g)
Soil leaching	-9.7_a ($mol/m^2/s$)	$1.6 \times 10^{-6}{}_b$
Denitrification	-10.0_a ($mol/m^2/s$)	$7.5 \times 10^{-5}{}_b$
Plant uptake	-8.0_b (L/s)	

199 Note: [a] Regnier and Steefel (1999); [b] calibrated values;

200

S4. Calibrated hydrology and water budget at Shale Hills

202 The spatially implicit model well reproduced the seasonal dynamics of discharge
203 and ET (Figure S9), with daily Nash-Sutcliffe efficiency (NSE) of 0.56 and 0.66,
204 respectively. Precipitation occurs throughout the year while the discharge was responsive
205 to a few big storm events in the spring and fall. The ET peaked during the summer due
206 to higher solar radiation and higher temperatures while declined in the fall and winter. The
207 runoff ratio was 0.46, suggesting 46% of precipitation is discharged through the stream
208 while the remaining 54% contributed to ET. A breakdown analysis suggests at the annual
209 scale, the subsurface lateral flow (Q_L, 87% of Q) dominated discharge, followed by the
210 deeper groundwater flow (Q_G, 9.3%) and the surface runoff (Q_S, 4.2%). Although Q_G was
211 not the largest component, it is essential in maintaining discharge during dry time,
212 especially in the summer.
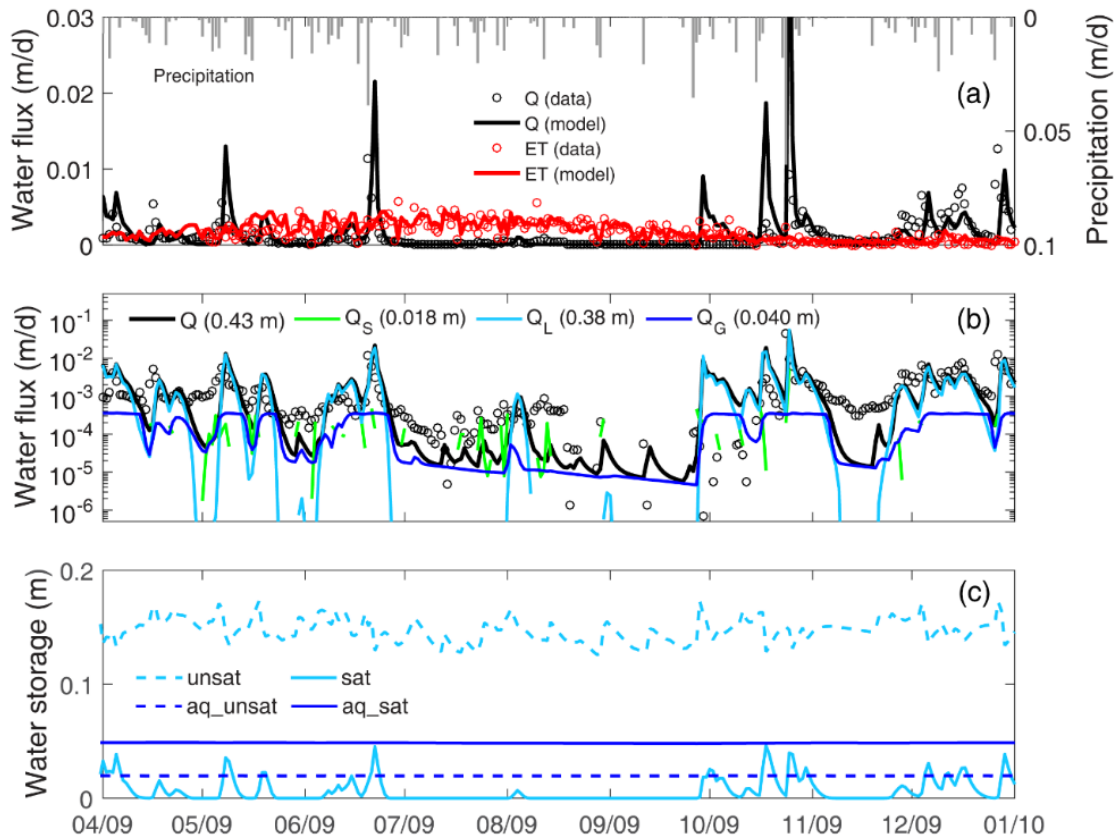
213

214 **Figure S9.** Hydrology and water flux at Shale Hills: (a) discharge and ET dynamics (data vs.

215 model); (b) discharge components of surface runoff (Q_s), shallow lateral flow (Q_L), and deep

216 groundwater (Q_G); (c) water storage of unsaturated and saturated zone in the soil and aquifer

217 layer.

218

219

220

221

222

223

224

225

226

227

Reference

Brantley, S. L., White, T., West, N., Williams, J. Z., Forsythe, B., Shapich, D., Kaye, J., Lin, H., Shi, Y. N., Kaye, M., Herndon, E., Davis, K. J., He, Y., Eissenstat, D., Weitzman, J., DiBiase, R., Li, L., Reed, W., Brubaker, K., and Gu, X.: Susquehanna Shale Hills Critical Zone Observatory: Shale Hills in the Context of Shaver's Creek Watershed, Vadose Zone Journal, 17, 1-19, ARTN 180092, 10.2136/vzj2018.04.0092, 2018.

Chiou, C. T., Lee, J. F., and Boyd, S. A.: The surface area of soil organic matter, Environmental Science & Technology, 24, 1164-1166, 1990.

Hasenmueller, E. A., Gu, X., Weitzman, J. N., Adams, T. S., Stinchcomb, G. E., Eissenstat, D. M., Drohan, P. J., Brantley, S. L., and Kaye, J. P.: Weathering of rock to regolith: The activity of deep roots in bedrock fractures, Geoderma, 300, 11-31, 2017.

Heidari, P., Li, L., Jin, L., Williams, J. Z., and Brantley, S. L.: A reactive transport model for Marcellus shale weathering, Geochimica et Cosmochimica Acta, 217, 421-440, 2017.

Kuntz, B. W., Rubin, S., Berkowitz, B., and Singha, K.: Quantifying Solute Transport at the Shale Hills Critical Zone Observatory, Vadose Zone Journal, 10, 843-857, 10.2136/vzj2010.0130, 2011.

Li, L., Salehikhoo, F., Brantley, S. L., and Heidari, P.: Spatial zonation limits magnesite dissolution in porous media, Geochimica et Cosmochimica Acta, 126, 555-573, 10.1016/j.gca.2013.10.051, 2014.

Li, L., Bao, C., Sullivan, P. L., Brantley, S., Shi, Y., and Duffy, C.: Understanding watershed hydrogeochemistry: 2. Synchronized hydrological and geochemical processes drive stream chemostatic behavior, Water Resources Research, 53, 2346-2367, 2017.

Regnier, P., and Steefel, C. I.: A high resolution estimate of the inorganic nitrogen flux from the Scheldt estuary to the coastal North Sea during a nitrogen-limited algal bloom, spring 1995, Geochimica et Cosmochimica Acta, 63, 1359-1374, 10.1016/s0016-7037(99)00034-4, 1999.

Rutherford, D. W., Chiou, C. T., and Kile, D. E.: Influence of soil organic matter composition on the partition of organic compounds, Environmental science & technology, 26, 336-340, 1992.

Shi, Y., Davis, K. J., Duffy, C. J., and Yu, X.: Development of a coupled land surface hydrologic model and evaluation at a critical zone observatory, Journal of Hydrometeorology, 14, 1401-1420, 2013.

Steefel, C., Appelo, C., Arora, B., Jacques, D., Kalbacher, T., Kolditz, O., Lagneau, V., Lichtner, P., Mayer, K. U., and Meeussen, J.: Reactive transport codes for subsurface environmental simulation, Computational Geosciences, 19, 445-478, 2015.

Steefel, C. I., and Lasaga, A. C.: A coupled model for transport of multiple chemical species and kinetic precipitation/dissolution reactions with application to reactive flow in single phase hydrothermal systems, American Journal of science, 294, 529-592, 1994.

Weitzman, J. N., and Kaye, J. P.: Nitrogen Budget and Topographic Controls on Nitrous Oxide in a Shale-Based Watershed, Journal of Geophysical Research: Biogeosciences, 123, 1888-1908, 2018.